Constraints on small-scale cosmological fluctuations from SNe lensing dispersion

Ido Ben-Dayan[1] and Ryuichi Takahashi[2]

[1]*Deutsches Elektronen-Synchrotron DESY, Theory Group, D-22603 Hamburg, Germany*
[2] *Faculty of Science and Technology, Hirosaki University, 3 Bunkyo-cho, Hirosaki, Aomori 036-8561, Japan*

ABSTRACT

We provide predictions on small-scale cosmological density power spectrum from supernova lensing dispersion. Parameterizing the primordial power spectrum with running α and running of running β of the spectral index, we exclude large positive α and β parameters which induce too large lensing dispersions over current observational upper bound. We ran cosmological N-body simulations of collisionless dark matter particles to investigate non-linear evolution of the primordial power spectrum with positive running parameters. The initial small-scale enhancement of the power spectrum is largely erased when entering into the non-linear regime. For example, even if the linear power spectrum at $k > 10h\mathrm{Mpc}^{-1}$ is enhanced by $1-2$ orders of magnitude, the enhancement much decreases to a factor of $2-3$ at late time ($z \leqslant 1.5$). Therefore, the lensing dispersion induced by the dark matter fluctuations weakly constrains the running parameters. When including baryon-cooling effects (which strongly enhance the small-scale clustering), the constraint is comparable or tighter than the PLANCK constraint, depending on the UV cut-off. Further investigations of the non-linear matter spectrum with baryonic processes is needed to reach a firm constraint.

Key words: cosmology: theory - gravitational lensing: weak - large-scale structure of the universe - cosmological parameters - inflation

1 INTRODUCTION

The plethora of cosmological observations has turned Cosmology into a quantitative science. From combining several probes that observe the Universe at different epochs and have different systematics and statistics, emerged the 'Concordance Model' of Cosmology, a six parameter model, most of them measured to the accuracy of a percent. Among these probes, type Ia supernovae (SNe) are a powerful cosmological tool to directly measure the expansion history of the Universe (see e.g. a recent review of Weinberg et al. 2013). The type Ia SNe are known as standard candles and one can measure the luminosity distances to them accurately. Several SNe surveys have set strong constraints on cosmological models from the distance-redshift relation (e.g. Riess et al. 1998; Perlmutter et al. 1999; Riess et al. 2007; Sullivan et al. 2011; Campbell et al. 2013). However the measured apparent magnitudes, have a residual scatter arising from its intrinsic scatter and effects due to line-of-sight (LOS) structures. The intrinsic scatter (~ 0.4 mag) can be significantly reduced to ~ 0.1 mag by empirically calibrating the luminosity curves. The scatter due to photon deflection along the line of sight is composed of many different physical effects. The dominant effects are peculiar velocities at $z < 0.1$ and gravitational lensing at $z \gtrsim 0.3$. Within the realm of cosmological perturbation theory and the stochastic nature of the LOS structures, all effects are expressed as an integral over the power spectrum with appropriate kinematical

factors (Ben-Dayan et al. 2012). The lensing effects create residuals from the best-fitting curve in the magnitude-redshift relation. The lensing magnifications of SNe can be extracted by correlating the residuals with the surface densities of nearby foreground galaxies. The lensing dispersion is roughly proportional to the SNe redshift z as $\sim 0.06z$ mag (e.g. Holz & Linder 2005; Ben-Dayan et al. 2013).

Detection of the lensing magnifications has been reported by several groups (Jönsson et al. 2006, 2010; Kronborg et al. 2010; Karpenka et al. 2013; Smith et al. 2014). Jönsson et al. (2010, hereafter J10) used a sample of 175 SNe at $0.2 \lesssim z \lesssim 1$ from the SNLS 3yr data, and measured SNe lensing magnifications by correlating the SNe fluxes and its foreground nearby galaxies (modeled as singular isothermal spheres). Modelling the lensing dispersion as $\sigma_{\mathrm{m}}(z_{\mathrm{s}}) = B z_{\mathrm{s}}$, they obtained a constraint $B \simeq 0.055^{+0.039}_{-0.041}$ mag (1σ) and an upper bound $B \lesssim 0.095(0.12)$ mag with $1(2)$-sigma confidence. More recently the Joint Lightcurve Analysis (JLA) (Betoule et al. 2014) combined SNe from various observations to compile 740 SNe for cosmological parameter inference, yielding $\Omega_{\mathrm{m}} = 0.295 \pm 0.034$ very close to the PLANCK result (Ade et al. 2015). The JLA did the following errors analysis. First it considered the peculiar velocity dispersion, that is relevant only for very low redshift. In addition, it used J10 central value for the lensing dispersion. Last, it considered all additional possible sources of error and named it 'coherent dispersion', σ_{coh}. Adding all of these

in quadrature produced the *total* dispersion, $\sigma_{\text{tot}}(z \leqslant 1) \leqslant 0.12$ in magnitude. There is also a clear trend of the total dispersion decreasing with redshift, Fig. 7 in JLA, suggesting that lensing might even be smaller than J10 central value. [1] Throughout the paper we will take this number $\sigma_{\text{m}} \leqslant 0.12$ as a conservative upper bound of the lensing dispersion, and $\sigma_{\text{m}} \leqslant 0.095$ as a 'plausible' upper bound, based on 1σ of J10.

The photons' scatter *biases* the measurement. However, given a cosmological model, we can use gravitational lensing as a *probe* of Cosmology and Astrophysics. There are several advantages of using SNe lensing as a cosmological probe. First, it has different systematics than other probes. Second, it is sensitive to different scales. For example, we shall see that lensing dispersion is mainly sensitive to $10^{-2} h\text{Mpc}^{-1} \leqslant k \leqslant 10^3 h\text{Mpc}^{-1}$. Third, even current data (or upper bound) is sufficient to constrain the cosmological parameters. The gravitational lensing of type Ia SNe has been suggested as a probe of cosmological abundance of compact objects (e.g. Rauch 1991; Holz 1998, 2001; Metcalf & Silk 1999; Mörtsell et al. 2001; Minty et al. 2002; Metcalf & Silk 2007; Yoo et al. 2008) and for measuring the present amplitude of matter density fluctuations (e.g. Metcalf 1999; Hamana & Futamase 2000; Valageas 2000; Dodelson & Vallinotto 2006; Marra et al. 2013; Quartin et al. 2014; Fedeli & Moscardini 2014; Iwata & Yoo 2015). For instance, Castro & Quartin (2014) recently measured σ_8 (the present amplitude of density fluctuations at $8h^{-1}\text{Mpc}$) using the non-Gaussianity of SNe magnitude distribution from 700 SNe at $z < 0.9$.

Recently, Ben-Dayan & Kalaydzhyan (2014) used the lensing dispersion to constrain small-scale amplitude of primordial curvature perturbation. They modelled the primordial power spectrum using running $\alpha \equiv dn_s/d\ln k$ and running of running $\beta \equiv d^2 n_s/d\ln k^2$ of the spectral index, and then discussed an observational constraint on α and β from the lensing dispersion. A subsequent work considered other parameterizations of the primordial power spectrum, (Ben-Dayan 2014). Current observations (Ade et al. 2015) measure $n_s(k_0) \simeq 0.96$, for the parameterization $P_k = A_s(k/k_0)^{n_s(k_0)-1}$, where k_0 is a suitable "pivot scale". Focusing again on "running", we consider:

$$n_s(k) = n_s(k_0) + \frac{\alpha(k_0)}{2}\ln\frac{k}{k_0} + \frac{\beta(k_0)}{6}\left(\ln\frac{k}{k_0}\right)^2, \quad (1)$$

There is no compelling evidence for the more generalized form, but the best $\Delta\chi^2$, that takes into account the suppression of low multiples in the temperature anisotropies spectrum is with $\alpha = 0, \beta = 0.029$ (Ade et al. 2015).[2] Given a single canonical scalar field ϕ and a potential $V(\phi)$, the above observables can be described by the slow-roll parameters, or the potential and its derivatives at the

'CMB point':

$$n_s = 1 + 2\eta - 6\epsilon \qquad (2)$$

$$\alpha = 16\epsilon\eta - 24\epsilon^2 - 2\xi^2 \qquad (3)$$

$$\beta = -192\epsilon^3 + 192\epsilon^2\eta - 32\epsilon\eta^2 - 24\epsilon\xi^2 + 2\eta\xi^2 + 2\omega^3 \qquad (4)$$

$$\epsilon = \frac{1}{2}\left(\frac{V'}{V}\right)^2, \quad \eta = \frac{V''}{V}, \quad \xi^2 = \frac{V'V'''}{V^2}, \quad \omega^3 = \frac{V'^2 V^{(4)}}{V^2}$$

where prime denotes derivative with respect to the inflaton. The best constraints on α, β with $k_0 = 0.05\text{Mpc}^{-1}$, $n_s(k_0) \simeq 0.96$ are given by PLANCK (Planck Collaboration et al. 2014b; Ade et al. 2015). These analyses are only probing the range $H_0 \leqslant k \lesssim 1\,\text{Mpc}^{-1}$. The lensing dispersion, σ_{m} is sensitive to $0.01\text{Mpc}^{-1} \lesssim k \lesssim 10^3\,\text{Mpc}^{-1}$, thus giving access to $2-3$ more decades of the spectrum. Hence, $\sigma_{\text{m}}(z)$ is particularly sensitive to the quasi-linear and non-linear part of the spectrum. In terms of inflation, the direct measurement of $k \lesssim 1\,\text{Mpc}^{-1}$ corresponds to about 8 e-folds of inflation, leaving most of the power spectrum of ~ 60 e-folds out of reach. Hence, even after PLANCK there is still an enormous space of inflationary models allowed. It is therefore of crucial importance to infer as much of the spectrum as possible for a better inflationary model selection. The lensing dispersion constrains additional $4-7$ e-folds, yielding a total of $12-15$ e-folds.

The main limitation of the analysis in Ben-Dayan & Kalaydzhyan (2014) and Ben-Dayan (2014), was the knowledge of the non-linear power spectrum $k \gtrsim 1h\text{Mpc}^{-1}$ at late times $z < 2$, in the case of running α and running of running β. In the absence of numerical simulations with proper initial conditions, enhancement of power on non-linear scales was parameterized by the enhancement that occurs in the Concordance Model (i.e. $\alpha = \beta = 0$). In this paper, we overcome the main limitation of previous works. We ran N-body simulations with non-zero α, β and derive a modified HaloFit formula for the non-linear power spectrum. We calculate the lensing dispersion and compare it with the observational upper bound $\sigma_{\text{tot}} \leqslant 0.12$. Then, large positive running parameters α and β can be rejected. We will also include the baryonic cooling effects, which strongly affect the small-scale clustering, in our investigation.

Before outlining the rest of the manuscript a valid question arises regarding the logic of considering just the lensing dispersion, rather than the full lensing probability distribution function (pdf). The calculated and experimentally quoted lensing dispersion is that of the distance modulus, $m \sim -2.5\log_{10} F$. The flux F is usually simplified to have a log-normal distribution (Holz & Linder 2005). In that case, the distance modulus is a Gaussian random variable and all the information is contained in the dispersion, and one does not need to consider higher moments of the pdf. Consideration of higher moments is relevant for deviations from the log-normal distribution of the flux and is beyond he scope of this work.

The paper is organized as follows. In sec.2, we briefly describe the lensing dispersion formula. In sec.3, we first present the primordial power spectrum parameterized with the running parameters (α and β), and then run the cosmological N-body simulations to follow its non-linear evolution accurately. The fitting formula of the non-linear matter power spectra are presented in this section and in the Appendix. Sec.4 presents our main results of the lensing dispersion and observational constraints on the running parameters. Here, we also include the baryon cooling effects. Conclusions and a discussion are in section 5. Throughout this paper we adopt the concordance ΛCDM model, which is consistent with the PLANCK results (Planck Collaboration et al. 2014a). The model is characterized by the matter density $\Omega_{\text{m}} = 0.3134$, the baryon density

---

[1] While the lensing dispersion grows with redshift, it is by no means the only contribution to the dispersion that can evolve with redshift. For example the SNe population can in principle evolve with redshift degrading the efficiency of SNe lensing as a probe. We thank Adam Riess for raising this issue.

[2] Non-trivial running is a *prediction* if ϵ is non monotonic, see Ben-Dayan & Brustein (2010), and a Higgs inflation version in Hamada et al. (2014); Bezrukov & Shaposhnikov (2014).

$\Omega_{\rm b} = 0.0486$, the cosmological constant density $\Omega_{\Lambda} = 0.6866$, the amplitude and the spectral index of primordial curvature power spectrum $A_{\rm s} = 2.20 \times 10^{-9}$, $n_{\rm s} = 0.96$, and the Hubble expansion rate today $H_0 = 67.3 \text{ km s}^{-1} \text{ Mpc}^{-1}$. We have verified that varying the other cosmological parameters does not change the conclusions beyond the quoted error bars (see Ben-Dayan & Kalaydzhyan 2014).

2 LENSING DISPERSION

When a distant SNe is gravitationally lensed by intervening structures, its flux is multiplied by a magnification factor μ and its apparent magnitude (or distance modulus) is changed by $\delta m = -2.5 \log_{10} \mu$. For a perturbed FLRW Universe, in the Poisson gauge, one starts with the line of sight (LOS) first order lensing contribution to the distance modulus,

$$\delta m(\eta_s^{(0)}) = \frac{5}{\ln 10} \int_{\eta_s^{(0)}}^{\eta_o} \frac{d\eta_1}{\Delta\eta} \frac{\eta_1 - \eta_s^{(0)}}{\eta_o - \eta_1} \Delta_2 \Psi \,, \qquad (5)$$

where the gravitational potential $\Psi = \Psi(\eta_i, r_i, \tilde{\theta}^a)$ is evaluated along the past light-cone at $r_i = \eta_o - \eta_i$, η_o is the observer conformal time, $\eta_s^{(0)}$ is the conformal time of the source with unperturbed geometry, $\Delta\eta(z) = \eta_o(z) - \eta_s^{(0)}(z) = H_0^{-1} \int_0^z dy/\sqrt{\Omega_{\rm m}(1+y)^3 + \Omega_{\Lambda}}$ and Δ_2 is the 2D angular Laplacian, see Ben-Dayan et al. (2012); Ben-Dayan et al. (2013) for technical terms and further explanations. Squaring (5) and taking the ensemble average in Fourier space at a fixed observed redshift, gives the variance, $\sigma_{\rm m}^2(z)$. The double LOS integral at $z \gtrsim 0.3$, is dominated by the equal time part, and with $\text{Si}(x \gg 1) \approx \pi/2$, gives:

$$\sigma_{\rm m}^2 \simeq \left(\frac{5}{\ln 10}\right)^2 \frac{\pi}{\Delta\eta^2} \int_{\eta_s^{(0)}}^{\eta_o} d\eta_1 \int dk P_{\Psi}(k, \eta_1) k^2 \qquad (6)$$
$$\times (\eta_1 - \eta_s^{(0)})^2 (\eta_o - \eta_1)^2 \,,$$

where P_{Ψ} is the dimensionless power spectrum of the *gravitational potential*. Hence, the lensing dispersion of supernovae is a direct measurement of the integrated late-time power spectrum. Let us stress that it is both UV and IR finite (Ben-Dayan et al. 2013). In general, the k^2 enhancement makes $\sigma_{\rm m}$ a sensitive probe to the small scales of the power spectrum. This sensitivity is manifest if we switch to dimensionless variables, $\tilde{\eta} = H_0 \eta$ and $p = k/k_{\rm eq}$:

$$\sigma_{\rm m}^2 \simeq \left(\frac{5}{\ln 10}\right)^2 \frac{\pi}{\Delta\tilde{\eta}^2} \left(\frac{k_{\rm eq}}{H_0}\right)^3 \int d\tilde{\eta}_1 \int dp P_{\Psi}(p, \tilde{\eta}_1) p^2 \quad (7)$$
$$\times (\tilde{\eta}_1 - \tilde{\eta}_s^{(0)})^2 (\tilde{\eta}_o - \tilde{\eta}_1)^2 \,.$$

It is easy to see that: (a) The relevant physical scales are H_0 and $k_{\rm eq}$, which give an enhancement of $(k_{\rm eq}/H_0)^3$. (b) The dispersion is really sensitive to scales smaller than the equality scale $p > 1$. (c) The nonlinear power spectrum (NLPS) has an additional redshift dependent physical scale which is the onset of nonlinearity $k_{\rm NL}$. For a given redshift, parameterizing the NLPS as $\sim C(k/k_{\rm NL})^{\nu}$, $\nu < -3$, from some $k_{\rm NL}$, will have an additional parametric enhancement of $(k_{\rm NL}/k_{\rm eq})^3$ to the lensing dispersion. Note that $\sigma_{\rm m}$ is in units of magnitude and the dispersion in equations (6) and (7) is *exactly* the standard result in weak gravitational lensing (e.g. Bartelmann & Schneider 2001). In principle, the lensing dispersion can probe the density fluctuations from a size of SNe at its maximum luminosity ($\approx 10^{15}$ cm) (e.g. Metcalf & Silk 1999;
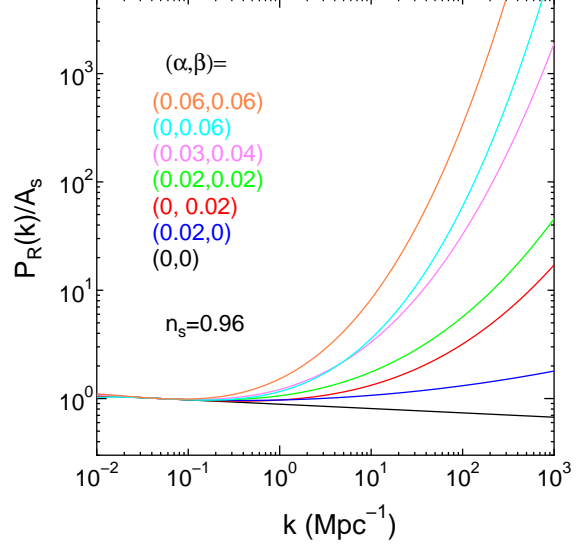
Figure 1. Dimensionless curvature power spectrum $\mathcal{P}_{\mathcal{R}}(k)$ in our running spectral index models: $(\alpha, \beta) = (0.06, 0.06), (0, 0.06), (0.03, 0.04), (0.02, 0.02), (0, 0.02), (0.02, 0), (0, 0)$ from top to bottom. Here, in vertical axis, the power spectrum is divided by its amplitude $A_{\rm s}$.

Mörtsell et al. 2001) to the present Horizon scale H_0^{-1}. From equation (7), it is clear that large scales $k < k_{\rm eq}$ have a negligible contribution. At smaller scales, $k \sim 1\,h\text{Mpc}^{-1}$, perturbation theory breaks down. Additionally, we expect non-Gaussian effects to become relevant. Last, the Nyquist wave number of the simulations soon to be discussed is at most $k_{\rm Nyq} = 64.3 h\text{Mpc}^{-1}$. We therefore limit the integration at most to $= 10^3 h\text{Mpc}^{-1}$, while $k_{\rm min} = H_0$.

In the following sections, we will evaluate the non-linear matter power spectrum using cosmological N-body simulations. Here, the (dimensional) matter power spectrum $P_{\rm m}$ and the (dimensionless) gravitational potential power spectrum P_{Ψ} are related via,

$$P_{\Psi}(k, z) = \frac{9}{8\pi^2} H_0^4 \Omega_{\rm m}^2 (1+z)^2 k^{-1} P_{\rm m}(k, z). \qquad (8)$$

3 NON-LINEAR MATTER POWER SPECTRUM

We run cosmological N-body simulations to investigate the non-linear matter power spectra of the various running spectral index models. Our purpose is to obtain a fitting formula of the non-linear power spectra and calculate the lensing dispersion in equation (6).

3.1 Linear power spectra with running spectral indices

The dimensionless curvature power spectrum is given by

$$\mathcal{P}_{\mathcal{R}}(k) = A_{\rm s} \left(\frac{k}{k_0}\right)^{n_{\rm s} - 1 + (\alpha/2)\ln(k/k_0) + (\beta/6)[\ln(k/k_0)]^2}, \qquad (9)$$

where $k_0 = 0.05 \text{Mpc}^{-1}$ is the PLANCK pivot scale, $A_{\rm s} = 2.20 \times 10^{-9}$ is the amplitude and $n_{\rm s} = 0.96$ is the spectral index. For the running α and the running of running β of the spectral index, we adopt seven models as $(\alpha, \beta) = (0, 0), (0, 0.02), (0.02, 0), (0.02, 0.02), (0.03, 0.04), (0, 0.06)$ and $(0.06, 0.06)$. Note that $A_{\rm s}$ is fixed for the running models ($\alpha \neq 0$, $\beta \neq 0$). Then, the present mass variance σ_8 at $8 h^{-1}$Mpc weakly increases as the running parameters (α and β) increase: $\sigma_8 = 0.829$ for $(\alpha, \beta) = (0, 0)$,

0.831 for $(0, 0.02)$, 0.833 for $(0.02, 0)$, 0.835 for $(0.02, 0.02)$, 0.839 for $(0.03, 0.04)$, 0.834 for $(0, 0.06)$, 0.847 for $(0.06, 0.06)$, respectively. Fig.1 plots the curvature power spectrum in equation (9) in our running models. The small-scale enhancement of $\mathcal{P}_{\mathcal{R}}(k)$ is clearly prominent. Large α, β models strongly enhance $\mathcal{P}_{\mathcal{R}}(k)$ by an order of magnitude for $k \gtrsim 10 \, h\mathrm{Mpc}^{-1}$. The PLANCK results already excluded large running models of $(\alpha, \beta) = (0, 0.06)$ and $(0.06, 0.06)$ at 2σ level (Planck Collaboration et al. 2014b). However, it is useful to study the general feature of the non-linear gravitational evolution with such strong small-scale enhancement. Furthermore, it provides an independent crosscheck, to the PLANCK analysis, and as we have mentioned, it probes scales beyond PLANCK's reach.

We prepare the linear matter power spectrum with the running parameters, $P_{\mathrm{m,lin}}(k; \alpha, \beta)$, as follows. We first evaluate the linear power spectrum without the running $P_{\mathrm{m,lin}}(k; \alpha = 0, \beta = 0)$ using CAMB (Lewis et al. 2000). Then, simply multiplying a factor from equation (9) to the output of CAMB as,

$$P_{\mathrm{m,lin}}(k; \alpha, \beta) = P_{\mathrm{m,lin}}(k; \alpha = 0, \beta = 0)$$
$$\times \left(\frac{k}{k_0} \right)^{(\alpha/2)\ln(k/k_0) + (\beta/6)[\ln(k/k_0)]^2} . \quad (10)$$

3.2 Cosmological N-body simulations

We run cosmological numerical simulations of dark matter particles in cubic boxes with a side of $100 h^{-1}\mathrm{Mpc}$. In order to check the numerical resolution, we run high- and low-resolution simulations in which the number of particles are 2048^3 and 1280^3. The initial matter power spectrum is prepared following the procedure in section 3.1. The initial positions and velocities of particles are given at redshift $z_{\mathrm{init}} = 99$ based on second-order Lagrangian perturbation theory (Crocce et al. 2006; Nishimichi et al. 2009).

To follow the gravitational evolution of the dark matter particles, we employ a publicly available tree-PM code GreeM (Ishiyama et al. 2009, 2012). GreeM is tuned to accelerate the tree gravitational calculation, and it is fast especially in the strongly non-linear regime. The PM meshes are set to be $1024^3 (640^3)$ and the particle Nyquist wavenumbers (which is determined by the mean particle separation) are $k_{\mathrm{Nyq}} = 64.3(40.2) h\mathrm{Mpc}^{-1}$ for the high-(low-)resolution simulations. The small-scale enhancement seen in Fig.1 is included up to the Nyquist wavenumber ($k < k_{\mathrm{Nyq}}$) in the initial conditions of our simulation. In other words, the initial linear $P_{\mathrm{lim}}(k)$ is zero at $k > k_{\mathrm{Nyq}}$. The gravitational softening length is set to be 3% of the mean particle separation. The simulation snapshots are dumped at redshifts $z = 0, 0.3, 0.6, 1$ and 1.5. We prepare 3(6) independent realizations for the high-(low-)resolution simulations for each (α, β) model to reduce the sample variance. Our simulation settings are summarized in Table 1.

Fig.2 shows our simulation results of the matter power spectra with the various running parameters (α, β) at $z = 0, 0.3, 0.6, 1$ and 1.5. The blue diamonds (black filled circles) with error bars are the mean power spectra with the standard deviations obtained from the realizations of high-(low-)resolution simulations. The blue (black) dotted lines are the shot noise for the high-(low-)resolution simulations. The high-resolution results are slightly higher (about 10%) than the low-resolution ones especially at low redshifts $z \leqslant 0.6$. The initial $P_{\mathrm{m,lin}}(k)$ is exponentially enhanced for some large α and β, and hence the simulation results would strongly depend on the resolution especially at wavenumbers comparable to or larger than the Nyquist wavenumber. However the differences between the high- and low-resolution results are smaller than 20%

for $k = 3 - 300 h\mathrm{Mpc}^{-1}$ at $z = 0 - 1.5$. The red solid curves are our fitting formula based on the Halofit model for the ΛCDM model (Smith et al. 2003; Takahashi et al. 2012), but slightly modified for the running spectral index models. The Halofit agrees with the simulation results within $18.3(28.3)\%$ relative error for $k < 300(600) h\mathrm{Mpc}^{-1}$ at $z = 0 - 1.5$. Details of the fitting parameters are given in Appendix A.

As seen in the figure, the matter power spectrum $P_{\mathrm{m}}(k)$ with larger running parameters is further enhanced at small scales. For example, $P_{\mathrm{m}}(k)$ with $(\alpha, \beta) = (0.06, 0.06)$ and $(0.03, 0.04)$ are about 3 and 2 times larger than that without the running at $k = 50 h\mathrm{Mpc}^{-1}$. However, the enhancement is much less prominent than those seen in the linear power spectrum (see Fig.1) which shows $1 - 2$ orders of magnitude enhancement at $k > 10 h\mathrm{Mpc}^{-1}$. Our numerical results show that the small-scale enhancement in the initial $P_{\mathrm{m}}(k)$ are largely smeared out at late times. This result exhibits power transfers from large to small scales, via mode coupling, and thus suggests that the initial large-scale power mainly determines the non-linear small-scale power at late times. These power transfers in the non-linear gravitational evolution has been well studied for the models in which an initial $P_{\mathrm{m}}(k)$ has a peak (like a Gaussian) at a specific scale (e.g., Bagla & Padmanabhan 1997; Padmanabhan & Ray 2006; Bagla & Prasad 2009; Neyrinck & Yang 2013; Nishimichi et al. 2014) and in models where the initial $P_{\mathrm{m}}(k)$ is damped at small scale such as warm dark matter models (e.g., Little et al. 1991; White & Croft 2000; Smith & Markovic 2011; Viel et al. 2012; Inoue et al. 2015). Such a smearing of small-scale enhancement makes it difficult to discriminate the running parameters (α, β) from the nonlinear $P_{\mathrm{m}}(k)$.

Before closing this section, let us comment on effects of the primordial small-scale enhancement on a halo mass function. We compute the mass function by identifying haloes in the low-resolution simulations using standard friends-of-friends algorithm with linking length of 0.17 times the mean particle separation. Then, as expected, the strong running models predict more numerous small halos, but the differences of the mass functions among the seven models are only less than a factor 2 at $z = 0 - 1.5$. For example, even for the smallest halo of $4 \times 10^9 h^{-1} M_\odot$ (which contains 100 simulation particles), the largest running model ($\alpha = \beta = 0.06$) has about $2(1.4)$ times more haloes comparing to the no running model ($\alpha = \beta = 0$) at $z = 1.5(0)$. This result suggests that the primordial small-scale enhancement does not significantly affect the halo mass function at late time ($z \leqslant 1.5$).

4 RESULTS

This section presents our main results of an observational upper bound on the running parameters (α, β) from the lensing dispersion. First, subsection 4.1 gives the results based on the non-linear matter power spectra of dark matter fluctuations obtained in previous section. Then, subsection 4.2 includes baryonic effects on the matter power spectra and the lensing dispersion. We will show that the baryonic effects strongly enhance the lensing dispersion and tighten the upper bound on α and β.

4.1 Dark Matter Only

Fig.3 shows our results of the lensing dispersion for the various running parameters (α, β). Here, we numerically calculate the lensing dispersion in equation (6) using our fitting formula of $P_{\mathrm{m}}(k)$.
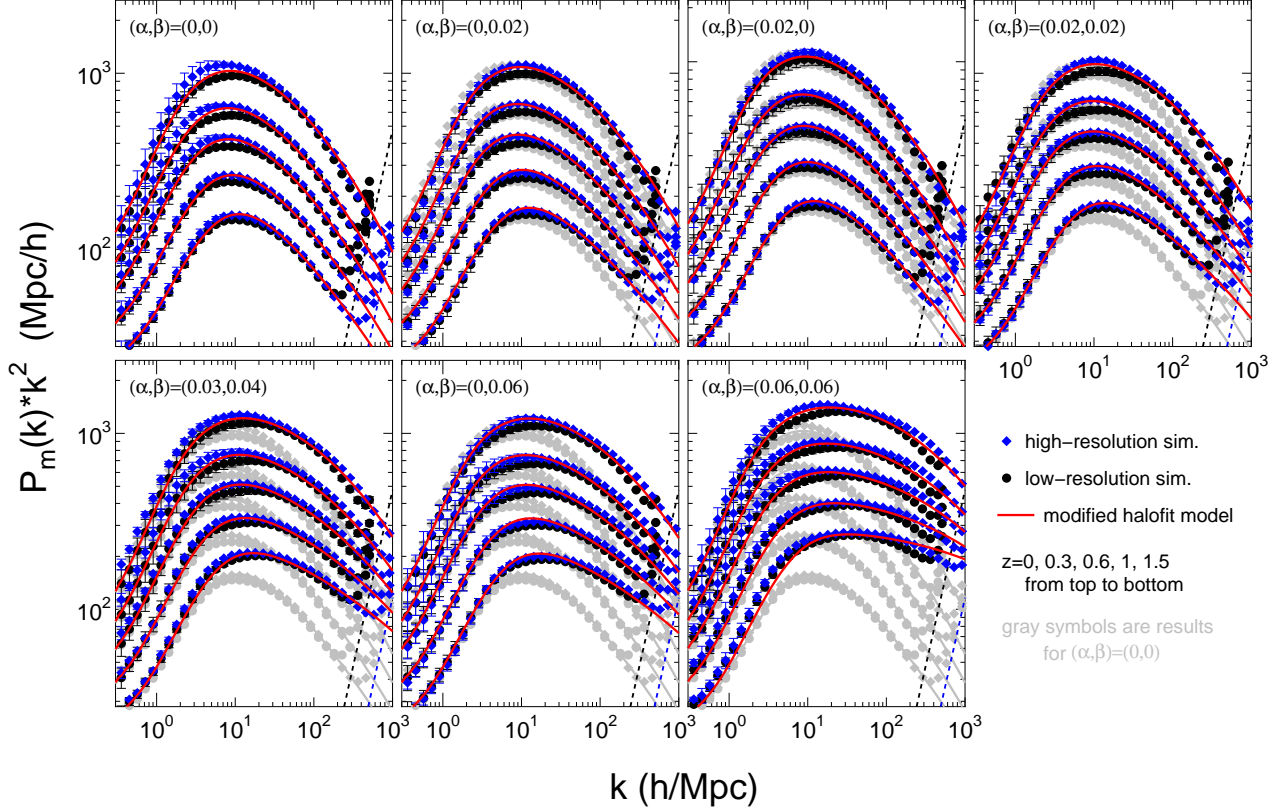
Figure 2. Non-linear matter power spectra with running α and running of running β of the spectral index. The seven panels correspond to $(\alpha, \beta) = (0, 0)$, $(0, 0.02)$, $(0.02, 0)$, $(0.02, 0.02)$, $(0.03, 0.04)$, $(0, 0.06)$ and $(0.06, 0.06)$, respectively. The redshifts are $z = 0, 0.3, 0.6, 1$ and 1.5 from top to bottom in each panel. In the vertical axis, the power spectrum is multiplied by a factor k^2 to show clearly our results. The blue diamonds (black filled circles) are the high-(low-)resolution simulation results. The dark gray symbols are the results for the no-running model $(\alpha, \beta) = (0, 0)$. The blue (black) dotted lines denote the shot noise in the high-(low-)resolution simulations. The red curves are our modified halofit model (see main text and Appendix A for detailed discussion).

Table 1. Our Simulation Setting

|	$L(h^{-1}\mathrm{Mpc})$	N_{p}^3	$k_{\mathrm{Nyq}}(h\mathrm{Mpc}^{-1})$	$m_{\mathrm{p}}(h^{-1}M_\odot)$	z	N_{r}
high-resolution	100	2048^3	64.3	1.0×10^7	$0, 0.3, 0.6, 1, 1.5$	3
low-resolution	100	1280^3	40.2	4.1×10^7	$0, 0.3, 0.6, 1, 1.5$	6

The different columns are the side length of simulation box L, the number of dark matter particles N_{p}^3, the Nyquist wavenumber k_{Nyq}, the particle mass m_{p}, the redshifts of the simulation outputs z, and the number of realizations N_{r}.

The figure clearly shows the lensing dispersion strongly depends on the running parameters. For instance, the lensing dispersion for the strongest running model ($\alpha = \beta = 0.06$) is about 40% higher than the Concordance Model ($\alpha = \beta = 0$) at $0 < z_{\mathrm{s}} \leqslant 2$. The bottom panel is the lensing dispersion divided by the source redshift, which shows $\sigma_{\mathrm{m}}(z_{\mathrm{s}})$ is roughly proportional to z_{s} at $z_{\mathrm{s}} \gtrsim 0.8$ (e.g. Holz & Linder 2005; Ben-Dayan et al. 2013).

We comment on the interval of the integration of the lensing dispersion. The integrand is proportional to $P_{\mathrm{m}}(k)k^2$ per $d\ln k$ from equations (6) and (8), and thus the contribution to the integral comes from the peak of $P_{\mathrm{m}}(k)k^2$ which corresponds to $k \approx 10h\mathrm{Mpc}^{-1}$ from Fig.2. Thus, the lensing dispersion does not strongly depend on the interval of the integral, if $k_{\mathrm{min}}(k_{\mathrm{max}})$ is much smaller (larger) than $\approx 10h\mathrm{Mpc}^{-1}$. For example, if we

set the maximum wavenumber $k_{\mathrm{max}} = 10^{10}h\mathrm{Mpc}^{-1}$, instead of $10^3 h\mathrm{Mpc}^{-1}$, the lensing dispersion becomes 6% larger for $\alpha = \beta = 0.06$ and less than 3% larger for the other models at $z_{\mathrm{s}} = 1$.

Fig.4 is a contour plot of the lensing dispersion at $z_{\mathrm{s}} = 1$ in $\alpha\beta$ plane. Here we apply our fitting formula of $P_{\mathrm{m}}(k)$ in a range of $0 < \alpha, \beta < 0.1$. The thin black lines correspond to $\sigma_{\mathrm{m}} = 0.07, 0.08, 0.09, \cdots$ (mag). The thick line ($\sigma_{\mathrm{m}} = 0.095$) corresponds to the observational upper bound (68% C.L.) from the Supernova Legacy Survey (SNLS, J10). White contours are PLANCK constraints of 1 and 2 sigma regions (Planck+WP+BAO in Planck Collaboration et al. 2014b). The dependence of α, β in σ_{m} (seen in the solid lines) comes from the fitting formula (A4), $3.32\alpha + 4.72\beta = $ const. Then, the SNLS constraint can be rewrit-
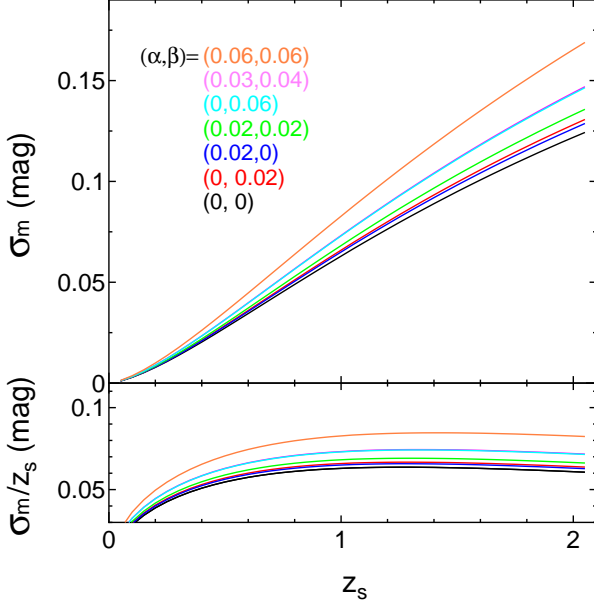
Figure 3. Lensing dispersion as a function of source redshift z_s for the various running α and running of running β of the spectral index. Top panel is the lensing dispersion in units of magnitude, and bottom one is the lensing dispersion divided by the source redshift.

Figure 4. Contour plot of the lensing dispersion at $z_s = 1$ in $\alpha\beta$ plane. The black solid lines correspond to $\sigma_m = 0.07, 0.08, 0.09, \cdots$ in steps of 0.01 (mag). The thick line ($\sigma_m = 0.095$) denotes the observational upper bound (1 sigma) from the Supernova Legacy Survey (J10). The white contours are the PLANCK (Planck Collaboration et al. 2014b) constraints of 1 and 2 sigma regions.

ten as $\alpha + 1.42\beta < 0.227$ (95% CL), and $\alpha + 1.42\beta < 0.167$ for the 'plausible upper bound' (68% CL). Our constraint may seem weaker than the PLANCK results, but it is important to note, that unlike CMB results, ours extend all the way to $k_{\max} = 10^3 h\mathrm{Mpc}^{-1}$. So while the result is not compelling as one may have hoped for, it still contains new information about the small scales of the primordial power spectrum in that it extends PLANCK constraints to the $k_{\max}$ scale, if lensing is actually observed.

Our numerical results of the lensing dispersion at $0.6 \leqslant z_s \leqslant 2$ and $0 \leqslant \alpha, \beta \leqslant 0.2$ can be fitted as,

$$\frac{\sigma_m(z_s; \alpha, \beta)}{z_s} = f_0(z_s) + f_1(z_s)\left\{x + f_2(z_s)x^{3.4}\right\}^{0.98} \quad \mathrm{mag} \tag{11}$$

where $x = 3.32\alpha + 4.72\beta$ and

$$f_0(z_s) = 0.061 + 0.010(z_s - 1) - 0.012(z_s - 1)^2,$$
$$f_1(z_s) = 0.038 + 0.003(z_s - 1),$$
$$f_2(z_s) = 0.75 + 0.37(z_s - 1) - 0.20(z_s - 1)^2. \tag{12}$$

The fitting function can reproduce the our numerical results within a relative error of 4.3% for $\sigma_m/z_s < 0.3$mag. Since σ_m is roughly proportional to z_s, z_s-dependencies of the functions $f_{0,1,2}(z_s)$ are relatively weak.

4.2 Including Baryonic Effects

In this subsection, we discuss the baryon-cooling effects on the matter power spectrum and the lensing dispersion. In our analysis, we adopt previous results of high-resolution hydrodynamic simulations to incorporate the baryonic effects into the lensing dispersion calculation. The baryon cooling naively enhances the matter power spectrum by some tens of percent at $k = 10 h\mathrm{Mpc}^{-1}$ and the enhancement is more significant for smaller scales (e.g. Jing et al. 2006; Rudd et al. 2008; Casarini et al. 2011). Recently,
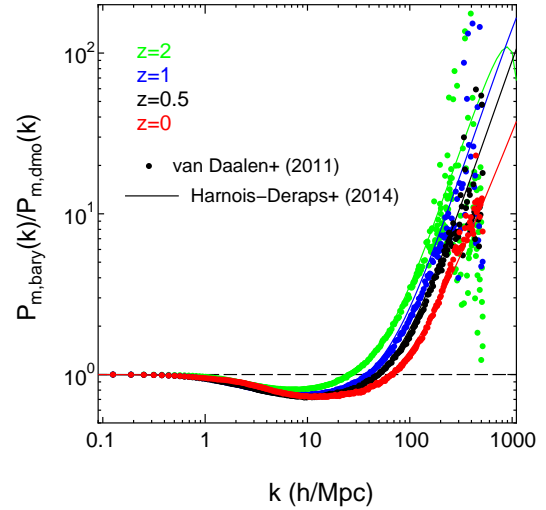
Figure 5. The baryon feedback bias in equation (13) at $z = 0, 0.5, 1$ and 2. The vertical axis is the power spectra with baryons divided by power spectra with dark matter only. The dots are simulation results of van Daalen et al. (2011) and the solid curves are the fitting formula of Harnois-Déraps et al. (2014).

two groups of the OverWhelmingly Large Simulations (OWLS) project (Schaye et al. 2010; van Daalen et al. 2011) and the Illustris project (Vogelsberger et al. 2014a,b) suggested that the AGN feedback suppressed $P_m(k)$ at intermediate scale ($k = 1 - 10 h\mathrm{Mpc}^{-1}$) but the baryon cooling strongly enhanced $P_m(k)$ by orders of magnitude at small scales ($k \gtrsim 100 h\mathrm{Mpc}^{-1}$). These previous numerical results are roughly consistent but slightly different from one another, since it strongly depends on modelling of compli-
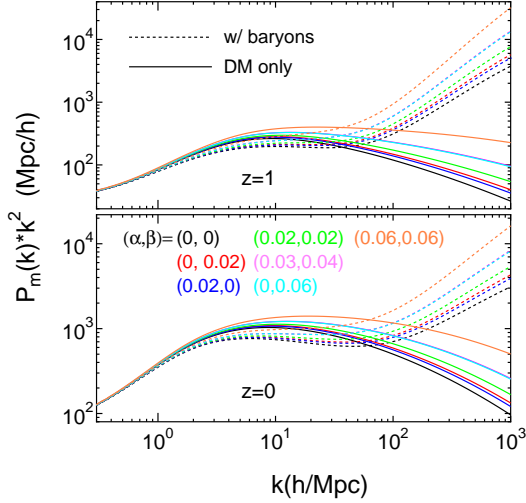
Figure 6. Matter power spectra with baryons (dotted curves) and without it (solid curves) at $z = 0$ and 1. The solid curves are our Halofit results, and the dotted curves are products of the baryon bias factor (13) times our Halofit results.

cated astrophysical process such as star formation, radiative cooling, supernova and AGN feedback. In this paper, we use the results of the most realistic model ("AGN_WMAP7") in the OWLS project. They used extended version of Gadget3 (Springel 2005) which used the treePM algorithm to calculate the gravitational evolution and smoothed particle hydrodynamics to follow the evolution of gas particles. They employed 512^3 CDM particles and equal number of baryonic particles in a cubic box of $100h\mathrm{Mpc}^{-1}$ on a side. Their Nyquist wavenumber is $16h\mathrm{Mpc}^{-1}$ and their softening length ($r_{\mathrm{soft}} = 7.8h^{-1}\mathrm{kpc}$) corresponds to a wavenumber $2\pi/r_{\mathrm{soft}} \simeq 800h\mathrm{Mpc}^{-1}$. They provided tabulated data of the matter power spectra up to $k \simeq 500h\mathrm{Mpc}^{-1}$ on their website [3]. Very recently, Harnois-Déraps et al. (2014) made a useful fitting formula of the matter power spectra with baryons obtained by the OWLS project. They fitted the ratio of the power spectra with baryons $P_{\mathrm{m,bary}}(k, z)$ to that with dark matter only $P_{\mathrm{m,dmo}}(k, z)$, called "the baryon feedback bias", which is defined as,

$$b_{\mathrm{bary}}^2(k, z) = \frac{P_{\mathrm{m,bary}}(k, z)}{P_{\mathrm{m,dmo}}(k, z)}. \tag{13}$$

Fig.5 plots the baryon feedback bias in Eq.(13) as a function of k at $z = 0, 0.5, 1$ and 2. As clearly seen in the figure, the AGN feedback suppresses the matter power spectrum at $k \approx 10h\mathrm{Mpc}^{-1}$ at some tens of percent, but the baryon cooling strongly enhances it at $k \gtrsim 100h\mathrm{Mpc}^{-1}$ by an order of magnitude. The fitting formula can reproduce the numerical results within 5% relative error for $k < 100h\mathrm{Mpc}^{-1}$ at $z < 1.5$ (Harnois-Déraps et al. 2014).

In this paper, we simply multiply the bias factor (13) to the results $P_{\mathrm{m}}(k)$ of our dark matter simulations to include the baryonic effects. The bias factor was obtained for WMAP 7yr cosmological model without the running spectral index (van Daalen et al. 2011). However, we assume that the baryon feedback bias does not depend on the running parameters α, β. Positive running α, β model probably enhances formations of small-scale clumps (such as dwarf galaxies and star clusters) at high redshift, which would affect the non-linear power spectrum. However, the dependence of the bias

on α, β is unknown at present and further investigations (hydrodynamical simulations with running spectral index) are necessary. Fig.6 shows the power spectra with baryons (dotted curves) and without it (solid curves) at $z = 0$ (lower panel) and $z = 1$ (upper one). In this figure, $P_{\mathrm{m,bary}}(k)k^2$ is a monotonically increasing function for large $k (\gtrsim 100h\mathrm{Mpc}^{-1})$ [4]. Thus, the integration in the lensing dispersion (6) strongly depends on k_{max} (it does not formally converge at $k_{\mathrm{max}} \to \infty$). In what follows, we will present the lensing dispersion results for several k_{max}.

Fig.7 shows the lensing dispersions with the baryons. Three panels are for various maximum wavenumbers in the integration (6), $k_{\mathrm{max}} = 300, 500$ and $1000h\mathrm{Mpc}^{-1}$ (where the maximum k_{max} is set to be $1000h\mathrm{Mpc}^{-1}$, because the fitting formula of the bias factor b_{bary}^2 becomes negative for $k > 1000h\mathrm{Mpc}^{-1}$ at high redshift $z > 2$ (Harnois-Déraps et al. 2014)). As expected, the results strongly depend on k_{max}. Depending on the chosen k_{max} various values of α, β are excluded, by the conservative (plausible) upper bound $\sigma_m(z \leqslant 1) \leqslant 0.12 \, (0.095)$.

Fig.8 is the contour plot of the lensing dispersion with the baryons at $z_s = 1$. The result σ_{m} for $k_{\mathrm{max}} = 300h\mathrm{Mpc}^{-1}$ is similar to the previous result in Fig.4, but σ_{m} is much larger than the previous results for $k_{\mathrm{max}} = 500$ and $1000 \, h\mathrm{Mpc}^{-1}$. The SNLS 1-(2-)sigma constraints can be rewritten as $\alpha + 1.42\beta < 0.145(0.222)$, $0.075(0.139)$ and $0.0006(0.054)$ for $k_{\mathrm{max}} = 300, 500$ and $1000h\mathrm{Mpc}^{-1}$, respectively. Our numerical results of $\sigma_{\mathrm{m}}(z_s; \alpha, \beta, k_{\mathrm{max}})$ at $0.6 \leqslant z_s \leqslant 2$ and $100h\mathrm{Mpc}^{-1} \leqslant k_{\mathrm{max}} \leqslant 1000h\mathrm{Mpc}^{-1}$ can be fitted as,

$$\frac{\sigma_{\mathrm{m}}(z_s; \alpha, \beta, k_{\mathrm{max}})}{z_s} = f_0(z_s, k_{\mathrm{max}}) \, e^{f_1(z_s, k_{\mathrm{max}})x + 1.8x^2} \quad \mathrm{mag} \tag{14}$$

where $x = 3.32\alpha + 4.72\beta$ and

$$f_0(z_s, k_{\mathrm{max}}) = \left[0.051 + 0.009(z_s - 1) - 0.009(z_s - 1)^2 \right]$$
$$\times (1 + 0.09k_{\mathrm{max},100}),$$
$$f_1(z_s, k_{\mathrm{max}}) = \left[0.046 + 0.017(z_s - 1) \right]$$
$$\times \left(1 + 5.38k_{\mathrm{max},100} - 0.27k_{\mathrm{max},100}^2 \right), \tag{15}$$

where $k_{\mathrm{max},100} = (k_{\mathrm{max}}/100h\mathrm{Mpc}^{-1})$. The fitting function agrees with our numerical results within a relative error of 8.7% for $0 \leqslant \alpha, \beta \leqslant 0.1$. A byproduct of this analysis, is an easy derivation of the validity of the baryon feedback. Taking $\alpha = \beta = 0$, we hit the dispersion upper bound of $\sigma(z \leqslant 1) \leqslant 0.12$ if we integrate up to $k_{\mathrm{max}} = 1500h\mathrm{Mpc}^{-1}$, while the 'plausible' $\sigma < 0.095$ is reached for $k_{\mathrm{max}} = 950h\mathrm{Mpc}^{-1}$. Hence the baryon bias has to be significantly modified and/or non-Gaussian effects have to be accounted for to explain the absence of detection of SNe lensing.

5 CONCLUSIONS AND DISCUSSION

We discussed the observational constraints on the small-scale power spectrum of the primordial curvature perturbation from SNe lensing dispersion. We modelled the common initial power spectrum with running parameters α and β of the spectral index, and ran

---

[3] http://vd11.strw.leidenuniv.nl/

---

[4] The original result of $P_{\mathrm{m,bary}}(k, z)k^2$ in the OWLS project is not an increasing function of k, rather roughly constant at $k \gtrsim 30h\mathrm{Mpc}^{-1}$. Their dark-matter simulation result $P_{\mathrm{m,dmo}}(k, z)$ is slightly smaller than ours at small scales ($k \gtrsim 100h\mathrm{Mpc}^{-1}$), which results in the difference of $P_{\mathrm{m,bary}}(k, z)$.
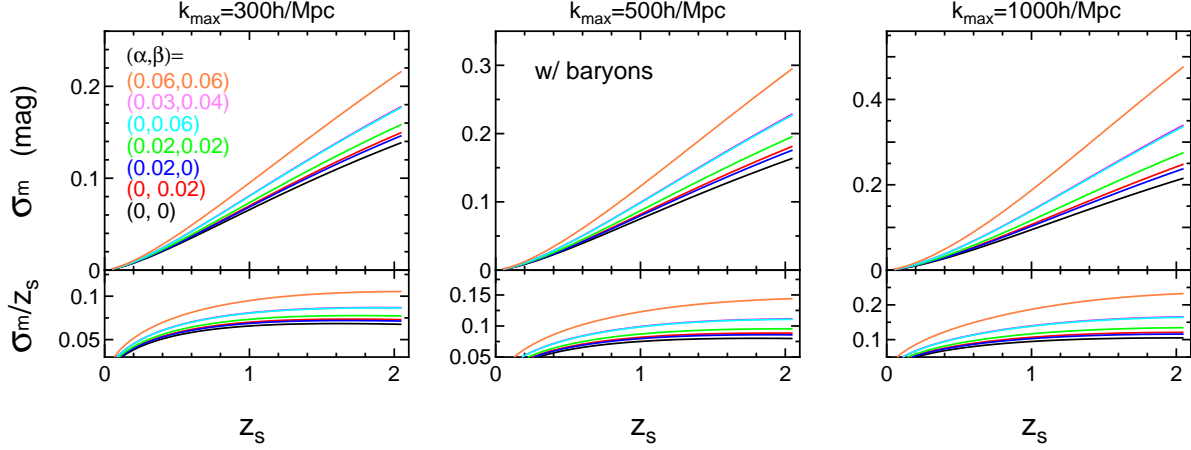
Figure 7. Same as Fig.3, but including baryonic effects on the matter power spectrum. Each panel corresponds to various maximum wave numbers in the integral of the lensing dispersion (6), $k_{\mathrm{max}} = 300, 500$ and $1000\,h\mathrm{Mpc}^{-1}$ from left to right. The baryons clearly enhance the lensing dispersion compared to the previous results in Fig.3.
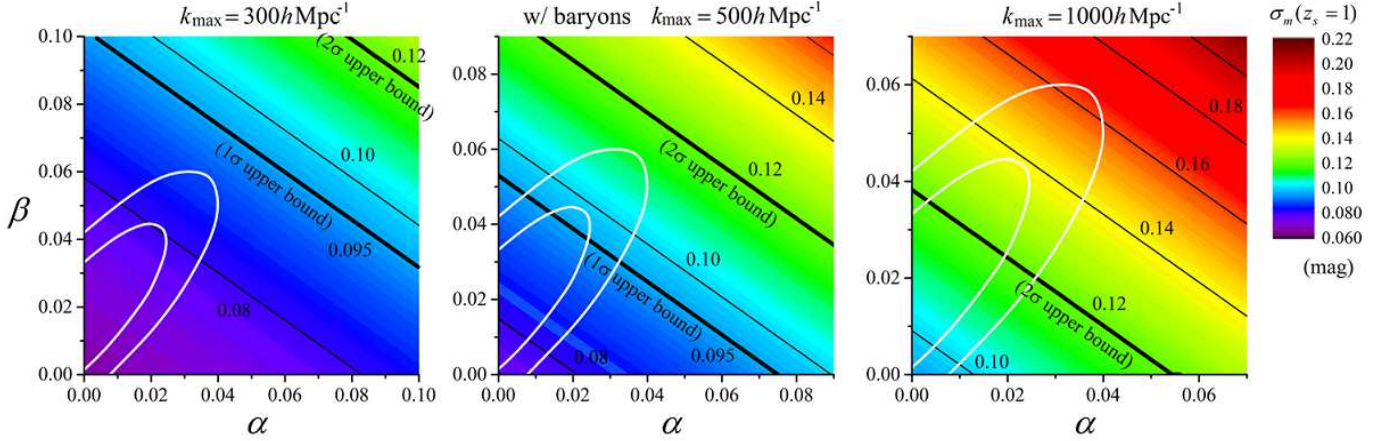
Figure 8. Same as Fig.4, but including baryonic effects on the matter power spectra. Each panel is for $k_{\mathrm{max}} = 300, 500$ and $1000\,h\mathrm{Mpc}^{-1}$ from left to right. Note again that the thick solid lines correspond to 1- and 2-sigma observational upper bounds from J10 and JLA, while the white contours are the PLANCK (Planck Collaboration et al. 2014b) 1 and 2 sigma likelihood contours.

the cosmological high-resolution N-body simulations to follow its non-linear evolution. We found that the small-scale enhancement in the primordial power spectrum is largely erased at late times during non-linear evolution, which suggests that it would be difficult to probe the small-scale primordial fluctuations using late time measurements. For the dark matter models, the observational constraints on α and β from the current observational data of the SNLS of JLA are weaker than the PLANCK results. However, if we include the baryonic effects, which strongly enhance the non-linear matter power spectrum at small-scales ($k \gtrsim 100h\mathrm{Mpc}$), the constraints are comparable to or tighter than PLANCK.

Let us discuss the accuracy of our Halofit formula in the high-k limit. The fitting formula was made to fit the simulation results in a finite range of $2h\mathrm{Mpc}^{-1} < k < 600h\mathrm{Mpc}^{-1}$ (see Appendix A). In the high-k limit, the simulation resolution limits the accuracy. In the initial particle distribution, the linear $P_{\mathrm{m}}(k)$ is included up to the Nyquist wavenumber k_{Nyq} and is exactly zero for $k > k_{\mathrm{Nyq}}$, and thus our simulation results may underestimate the non-linear

$P_{\mathrm{m}}(k)$ for $k > k_{\mathrm{Nyq}}$ at late times. Evidence for such an underestimation is the enhanced power spectrum in the high resolution simulations compared to the low resolution ones ($k_{\mathrm{Nyq}} = 64$ and $40\,h\mathrm{Mpc}^{-1}$, respectively). Additional hint for such an underestimation is that at some point the nonlinear power spectrum becomes smaller than the linear one for very large wavenumbers. For example at $k \simeq 1000\,h\mathrm{Mpc}^{-1}$ for $z = 0$, $\alpha = \beta = 0.03$ and at $k \simeq 120\,h\mathrm{Mpc}^{-1}$ for $z = 0$, $\alpha = \beta = 0.06$. This lack of resolution would degrade the accuracy at small-scales especially for large α, β models. However, as seen in Fig.2, the high- and low-resolution simulations with aforementioned Nyquist wave numbers, give similar results with less than 20% difference for $k < 300\,h\mathrm{Mpc}^{-1}$, suggesting the safe convergence of our simulations. Further studies investigating the non-linear $P_{\mathrm{m}}(k)$ with positive α, β at such smaller-scales are necessary.

As we have seen, baryonic effects strongly influence our conclusions. Baryonic simulation results strongly depend on assumptions about various astrophysical processes (star formation and

AGN feedback, stellar mass function and so on). Our results are based on two assumptions: i) We have used the van Daalen et al. (2011) results. (In other words, we assume that the simulation of van Daalen et al. (2011) is correct.) ii) The baryon feedback bias in (13) can be used even with large α and β. Then, under these assumptions, we can safely set the strong constraints. It may very well be that assumption ii) is incorrect, and simulations of baryons with initial α and β will produce a better behaved spectrum, similar to our dark matter simulation results. If our assumptions will be verified, it is clear that baryons have an overwhelming effect, as they induce $\mathcal{O}(1)$ changes of the power spectrum at $k \gtrsim 5\,h\mathrm{Mpc}^{-1}$. Furthermore, the changes in the power spectrum are non-monotonic in k. Last, with current simulation data, baryon cooling destroys the UV convergence, $P_{\mathrm{m}}(k)k^2$ diverges at $k \to \infty$, making the lensing dispersion a UV sensitive quantity. It is therefore senseless to derive conclusions on the power spectrum without the inclusion of baryons. Moreover, any (late-time) astrophysical probe that is sensitive to such scales, requires an accurate baryon modelling before deriving any conclusions about cosmology. As discussed in sec.4.2, we need high-resolution hydrodynamic simulations with various initial conditions, that can probe very small-scales to reach a firm conclusion. Given the huge effect of baryons on lensing dispersion, SNe lensing might be a useful calibrator for baryonic processes. Especially since inclusion of baryonic effects in the Concordance Model ($\alpha = \beta = 0$), implies a diverging power spectrum, that is unphysical, and gives a lensing dispersion very close to the observational bound for $k_{max} \sim 1000, h\mathrm{Mpc}^{-1}$.

Another natural development is considering higher moments of the lensing pdf. Including small-scale fluctuations, the probability distribution of the magnification would be strongly non-Gaussian (highly skewed). In fact, according to previous ray-tracing simulations in standard ΛCDM universe (e.g. Hilbert et al. 2007; Takahashi et al. 2011), the magnification PDF is rather a (modified) lognormal distribution with power-law tail at high μ. Hence, the simple dispersion would not be sufficient to describe the lensing effects, and then the higher-order statistics such as skewness and kurtosis provide independent useful information.

Finally, let us comment on future constraints on the running parameters α and β, and on the power spectrum at small scales. Current tightest constraint on α and β comes from PLANCK, which constrains them within $O(0.01)$ accuracy. Adding to the CMB observations, future radio telescopes measuring 21cm fluctuations such as the Square Kilometer Array[5] and the Omniscope[6] will constrain them within $O(0.001)$ accuracy (e.g. Mao et al. 2008; Kohri et al. 2013; Shimabukuro et al. 2014). Small-scale perturbations generate spectral distortions of CMB by Silk dumping due to photon diffusion, and future planned experiment PIXIE are also expected to probe the power spectrum up to scales as small as $k = 10^4 \mathrm{Mpc}^{-1}$, and potentially measure α, β. (Chluba et al. 2012; Powell 2012; Chluba & Jeong 2014). Given the baryonic effects that swamp late time measurements, it seems that such early universe measurements are more promising in that respect.

ACKNOWLEDGMENTS

REFERENCES

Ade P., et al., 2015, arXiv:1502.01589
Bagla J. S., Padmanabhan T., 1997, MNRAS, 286, 1023
Bagla J. S., Prasad J., 2009, MNRAS, 393, 607
Bartelmann M., Schneider P., 2001, Physics Report, 340, 291
Ben-Dayan I., 2014, arXiv:1408.3004
Ben-Dayan I., Brustein R., 2010, JCAP, 1009, 007
Ben-Dayan I., Gasperini M., Marozzi G., Nugier F., Veneziano G., 2013, JCAP, 6, 2
Ben-Dayan I., Kalaydzhyan T., 2014, Phys. Rev. D, 90, 083509
Ben-Dayan I., Marozzi G., Nugier F., Veneziano G., 2012, JCAP, 1211, 045
Betoule M., et al., 2014, Astron.Astrophys., 568, A22
Bezrukov F., Shaposhnikov M., 2014, Phys.Lett., B734, 249
Campbell H. et al., 2013, ApJ, 763, 88
Casarini L., Macciò A. V., Bonometto S. A., Stinson G. S., 2011, MNRAS, 412, 911
Castro T., Quartin M., 2014, MNRAS, 443, L6
Chluba J., Erickcek A. L., Ben-Dayan I., 2012, Astrophys.J., 758, 76
Chluba J., Jeong D., 2014, Mon.Not.Roy.Astron.Soc., 438, 2065
Crocce M., Pueblas S., Scoccimarro R., 2006, MNRAS, 373, 369
Dodelson S., Vallinotto A., 2006, Phys. Rev. D, 74, 063515
Fedeli C., Moscardini L., 2014, MNRAS, 442, 2659
Hamada Y., Kawai H., Oda K.-y., Park S. C., 2014, Phys.Rev.Lett., 112, 241301
Hamana T., Futamase T., 2000, ApJ, 534, 29
Harnois-Déraps J., van Waerbeke L., Viola M., Heymans C., 2014, arXiv:1407.4301
Hilbert S., White S. D. M., Hartlap J., Schneider P., 2007, MNRAS, 382, 121
Holz D. E., 1998, ApJ, 506, L1
Holz D. E., 2001, ApJ, 556, L71
Holz D. E., Linder E. V., 2005, ApJ, 631, 678
Inoue K. T., Takahashi R., Takahashi T., Ishiyama T., 2015, MNRAS, 448, 2704
Ishiyama T., Fukushige T., Makino J., 2009, PASJ, 61, 1319
Ishiyama T., Nitadori K., Makino J., 2012, Proc. Int. Conf. High Performance Computing, Networking, Storage and Analysis, SC '12 (Los Alamitos, CA: IEEE Computer Society Press), 5, (arXiv:1211.4406)
Iwata K., Yoo C.-M., 2015, EPL (Europhysics Letters), 109, 39001
Jing Y. P., Zhang P., Lin W. P., Gao L., Springel V., 2006, ApJ, 640, L119
Jönsson J., Dahlén T., Goobar A., Gunnarsson C., Mörtsell E., Lee K., 2006, ApJ, 639, 991

Jönsson J. et al., 2010, MNRAS, 405, 535

Karpenka N. V., March M. C., Feroz F., Hobson M. P., 2013, MN-RAS, 433, 2693

Kohri K., Oyama Y., Sekiguchi T., Takahashi T., 2013, JCAP, 10, 65

Kronborg T. et al., 2010, A.&Ap., 514, A44

Lewis A., Challinor A., Lasenby A., 2000, ApJ, 538, 473

Little B., Weinberg D. H., Park C., 1991, MNRAS, 253, 295

Mao Y., Tegmark M., McQuinn M., Zaldarriaga M., Zahn O., 2008, Phys. Rev. D, 78, 023529

Marra V., Quartin M., Amendola L., 2013, Phys. Rev. D, 88, 063004

Metcalf R. B., 1999, MNRAS, 305, 746

Metcalf R. B., Silk J., 1999, ApJ, 519, L1

Metcalf R. B., Silk J., 2007, Physical Review Letters, 98, 071302

Minty E. M., Heavens A. F., Hawkins M. R., 2002, Mon.Not.Roy.Astron.Soc., 330, 378

Mörtsell E., Goobar A., Bergström L., 2001, ApJ, 559, 53

Neyrinck M. C., Yang L. F., 2013, MNRAS, 433, 1628

Nishimichi T., Bernardeau F., Taruya A., 2014, arXiv:1411.2970

Nishimichi T. et al., 2009, Publ. Astron. Soc. Japan, 61, 321

Padmanabhan T., Ray S., 2006, MNRAS, 372, L53

Perlmutter S. et al., 1999, ApJ, 517, 565

Planck Collaboration et al., 2014a, A.&Ap., 571, A16

Planck Collaboration et al., 2014b, A.&Ap., 571, A22

Powell B. A., 2012, arXiv:1209.2024

Quartin M., Marra V., Amendola L., 2014, Phys. Rev. D, 89, 023009

Rauch K. P., 1991, ApJ, 374, 83

Riess A. G. et al., 1998, AJ, 116, 1009

Riess A. G. et al., 2007, ApJ, 659, 98

Rudd D. H., Zentner A. R., Kravtsov A. V., 2008, ApJ, 672, 19

Schaye J. et al., 2010, MNRAS, 402, 1536

Shimabukuro H., Ichiki K., Inoue S., Yokoyama S., 2014, Phys. Rev. D, 90, 083003

Smith M. et al., 2014, ApJ, 780, 24

Smith R. E., Markovic K., 2011, Physical Review D, 84, 063507

Smith R. E. et al., 2003, MNRAS, 341, 1311

Springel V., 2005, MNRAS, 364, 1105

Sullivan M. et al., 2011, ApJ, 737, 102

Takahashi R., Oguri M., Sato M., Hamana T., 2011, ApJ, 742, 15

Takahashi R., Sato M., Nishimichi T., Taruya A., Oguri M., 2012, ApJ, 761, 152

Valageas P., 2000, A.&Ap., 354, 767

van Daalen M. P., Schaye J., Booth C. M., Dalla Vecchia C., 2011, MNRAS, 415, 3649

Viel M., Markovic K., Baldi M., Weller J., 2012, MNRAS, 421, 50

Vogelsberger M. et al., 2014a, Nature, 509, 177

Vogelsberger M. et al., 2014b, MNRAS, 444, 1518

Weinberg D. H., Mortonson M. J., Eisenstein D. J., Hirata C., Riess A. G., Rozo E., 2013, Physics Report, 530, 87

White M., Croft R. A. C., 2000, ApJ, 539, 497

Yoo C., Ishihara H., Nakao K., Tagoshi H., 2008, Progress of Theoretical Physics, 120, 961

APPENDIX A: FITTING FORMULA FOR NON-LINEAR MATTER POWER SPECTRA

This Appendix presents our fitting formula for the matter power spectra with running and running of running of the spectral in-dex. Our formula is based on the halofit model (Smith et al. 2003; Takahashi et al. 2012, hereafter T12), but slightly modified for the running models.

To find the best fitting parameters in the halofit model, we use the standard chi-square analysis, which is defined as

$$\chi^2 = \sum_i \sum_{z=0}^{1.5} \sum_{k=k_{\min}}^{k_{\max}} \frac{[P_{i,\text{model}}(k,z) - P_{i,\text{sim}}(k,z)]^2}{P_{i,\text{sim}}(k,z)^2}, \quad \text{(A1)}$$

where $P_{i,\text{model}}$ is the power spectrum in the theoretical model, $P_{i,\text{sim}}$ is those in the simulation results, and i denotes the seven models of the running parameters (α, β). The χ^2 is summed over redshifts $z = 0, 0.3, 0.6, 1$ and 1.5. We use the wavenumber k larger than $2\,h\text{Mpc}^{-1}(= k_{\min})$ where the Gaussian error of $P(k)$ is less than 1%. We set the maximum wavenumber $k_{\max}$ so that the measured power spectrum is much larger (10 times larger) than the shot noise. Thus, $k_{\max}$ depends on the parameters of α, β and z. The maximum (minimum) $k_{\max}$ is $600(100)h\text{Mpc}^{-1}$ for $\alpha = \beta = 0.06(0)$ at $z = 0(1.5)$.

First, we fit the simulation results for the no running model ($\alpha = \beta = 0$). Here, we slightly modify the formula in T12. The halofit in T12 can be used up to $k < 30h\text{Mpc}^{-1}$ within 10% error, but it asymptotically overestimate the $P_{\text{m}}(k)$ at very large $k(> 100h\text{Mpc}^{-1})$. The fitting parameters are the same as in T12, except for the following two parameters:

$$\log_{10} c_{\text{n}} = -0.3370 + 2.1842 n_{\text{eff}} + 0.9604 n_{\text{eff}}^2 + 2.3764C,$$
$$\gamma_{\text{n}} = 0.1027 - 0.0219 n_{\text{eff}} + 2.6785C$$
$$- (0.2866 + 0.1206 n_{\text{eff}}) \ln\left(\frac{k}{h\text{Mpc}^{-1}}\right). \quad \text{(A2)}$$

In the last term, if one uses the wavenumber in unit of Mpc^{-1} (not $h\text{Mpc}^{-1}$), then one has to insert a specific value of h. The equation (A2) gives a minor correction to the formula in T12, which corrects the overestimation in T12 at $k > 100h\text{Mpc}^{-1}$. The $P_{\text{m}}(k)$ with and without the correction in equation (A2) are different within 17% for $k < 100h\text{Mpc}^{-1}$.

The ratios of the power spectra with the running to that without it are fitted as,

$$\frac{P(k,z;\alpha,\beta)}{P(k,z;\alpha=\beta=0)} = \left[1 + 0.123\left(\frac{k}{h\text{Mpc}^{-1}}\right)^{0.794}\right]^{p(z;\alpha,\beta)}, \quad \text{(A3)}$$

with

$$p(z;\alpha,\beta) = (3.32\alpha + 4.72\beta)(1+z)^{0.379} \quad \text{(A4)}$$

The RHS of equation (A3) corresponds to an enhancement factor. Note that the parameters n_{eff} and C in equation (A2) are evaluated in the no running model even when computing $P_{\text{m}}(k)$ for the running models. Using our fitting formula, the simulation results can be reproduced within a relative error of $18.3(28.3)\%$ for $k < 300(600)h\text{Mpc}^{-1}$ at $z = 0 - 1.5$. The root-mean-square deviation between the theoretical model and the simulation results is about 5.1%.

Fig.A1 shows the ratio of the power spectrum with the running, $P_{\text{m}}(k,z;\alpha,\beta)$, to that without it, $P_{\text{m}}(k,z;\alpha = 0, \beta = 0)$. The red solid curves show the enhancement of power spectra described by our fitting factor in Eq.(A3), which reproduces our simulation results very well.
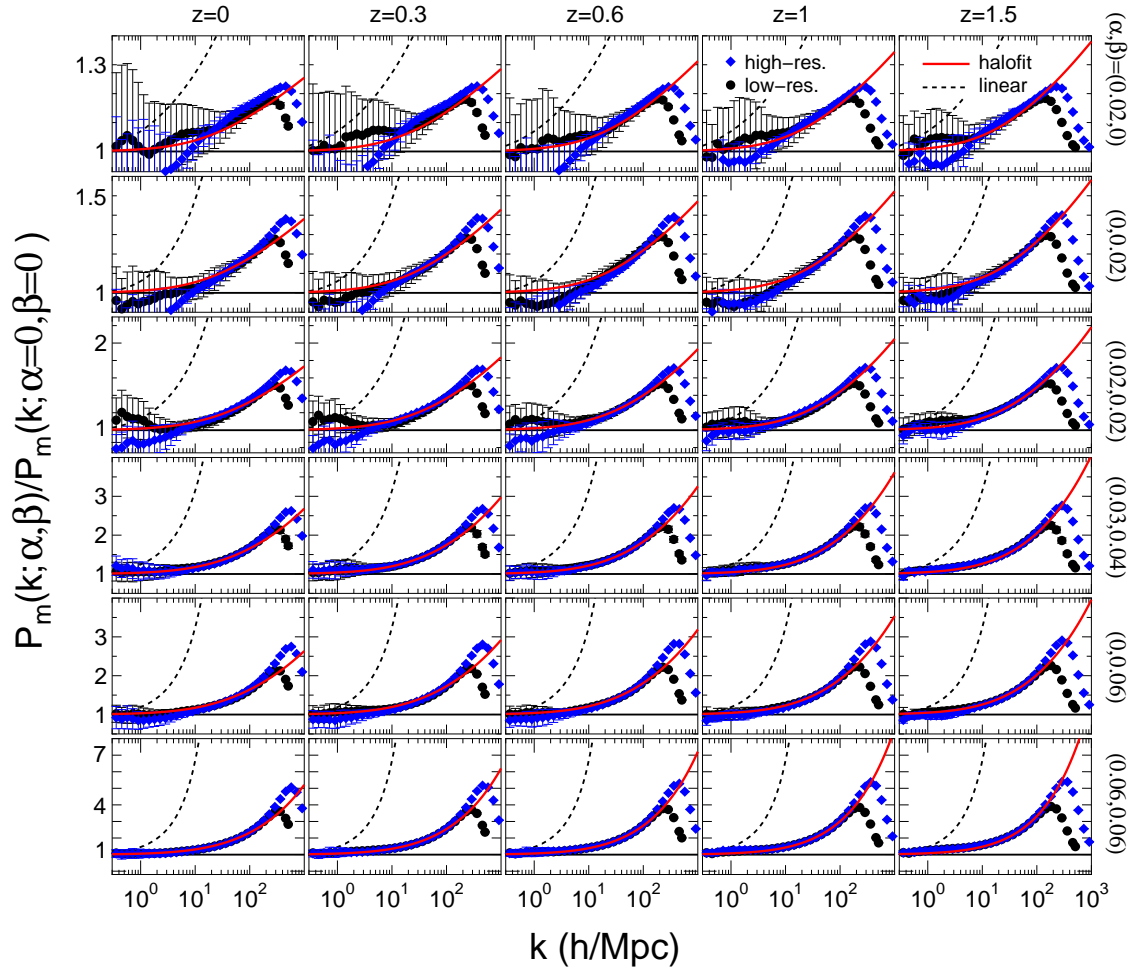
Figure A1. Ratio of the power spectra with the running $P_\mathrm{m}(k, z; \alpha, \beta)$ to that without the running $P_\mathrm{m}(k, z; \alpha = 0, \beta = 0)$. The blue diamonds (black dots) are the ratios in the high-(low-)resolution simulations. The dotted curves are the ratios in the linear power spectra. The red solid curves are our enhancement factor in equation (A3). The small dumping at very high $k(> 100 h\mathrm{Mpc}^{-1})$ of the simulation results are due to the shot noise in the denominator $P_\mathrm{m}(k, z; \alpha = 0, \beta = 0)$.